COMPARISON OF EXPERIMENTAL AND THEORETICAL ELECTRONIC CHARGE DISTRIBUTIONS IN γ-TiAl

Z. W. LU†, ALEX ZUNGER[1] and A. G. FOX[2]

[1]National Renewable Energy Laboratory, Golden, CO 80401 and [2]Materials Science Section, Department of Mechanical Engineering, United States Naval Postgraduate School, Monterey, CA 93943-5100, U.S.A.

Abstract—Using critical voltage electron diffraction, Fox has recently determined the lowest seven X-ray structure factors of γ-TiAl (L1$_0$ structure). We present here a comparison of these accurately measured (0.15%) structure factors with first-principles local density calculations, finding an agreement within 0.7% and an r.m.s. error of 0.013 e/atom. While such measurements are limited to the first few structure factors $\rho(G)$ (where G is the crystal momentum), theory is able to obtain $\rho(G)$ for arbitrarily high G. If we construct charge density deformation maps by Fourier summations up to the lowest measured G, the calculated and experimental density deformation maps agree very closely. However, if we include in the theoretical density deformation map high G values (outside the range accessible to experiment), qualitatively different bonding patterns appear, in particular between Ti atoms. Systematic study of the total, valence, and deformation charge densities as well as comparison with result for NiAl in the hypothetical L1$_0$ structure elucidate the bonding patterns in these transition metal aluminides.

1. INTRODUCTION

The bonding charge density in a solid is defined as the difference between the electron distribution in the crystal and that obtained from a superposition of spherically symmetric ground state atomic charge densities. This "deformation electron density difference" (DEDD) constitutes only a small fraction of the total charge density: in terms of the X-ray structure factor, it is often only ~1% or less of the total structure factor. Highly accurate measurements of structure factors are therefore needed to reliably determine the DEDD. Recent advances in diffraction techniques and data processing led to an unprecedented level of accuracy in determining the first few lowest structure factors (hence the DEDD) in solids such as Be [1], Al [2], GaAs [3], Si [4, 5] and NiAl [6] using X-ray, gamma-ray and electron diffraction and X-ray Pendellösung methods. For example, in the best studied case of Si, the X-ray Pendellösung method [4, 5] in conjunction with Dawson's method of refinement [5] led to an unprecedented accuracy of an *R*-factor of 0.036% and millielectron accuracy in individual structure factors. For the intermetallic compounds NiAl, electron diffraction experiment [6] have achieved an accuracy of 0.2% for the first few structure factors. These experimental developments have been recently matched by parallel refinements in first-principles local density [7–10] calculations for GaAs [11], Si [12, 13], C [13], Ge [13] and NiAl [14],

in which the traditional computational difficulties with convergence of the basis set, Brillouin-zone-sampling and self-consistency have been largely overcome. This is illustrated by the recent achievement of an *R*-factor of 0.2% between theory and experiment (differences in individual structure factors not exceeding 21 millielectron) for crystalline Si [12, 13].

This recent interplay between high-precision DEDD determinations by experiment and theory exposed a number of interesting features [11–14]:

(i) Accurate *ab initio* self-consistent local density calculations match very well the lowest few structure factors amenable to experimental determination.

(ii) However, contrary to what was originally expected [15], higher order structure factors, outside the reach of current high-precision measurements, can contribute significantly to the calculated DEDD. Hence, Fourier series truncations, necessitated by many of the current measurement and data processing techniques miss some of the *essential features* of the bonding even though the experimentally accessible low-order structure factors are now known very accurately.

(iii) This problem can be largely circumvented if instead of using a *truncated* Fourier series in constructing the experimental DEDD one extrapolates the measured structure factors by using a physically motivated charge density model. An example is the Dawson's model [16] recently applied successfully to Si [5, 13, 17], C [13] and Ge [13]. Unlike the more routine data processing models [18], this approach does not require that the charge density be represented by a superposition of *spherical* functions

---

alone. However, because of insufficient data, such clever approaches have not been applied yet to study the DEDD in *compounds*.

(iv) Quantitative first-principles calcualtions showed that many of the previously held intuitive expectations [3, 6, 15] on the magnitude and chemical trends in the DEDD are not supported. For example: (a) the Debye–Waller factor e^{-G^2B} does not attenuate sufficiently the high-momentum (G) structure factor differences to eliminate [3, 15] their effects on the DEDD maps. (b) The contribution to the charge density from bonding effects in relatively ionic inter-metallics (e.g. NiAl) are less than what was initially expected [6]. (c) The expectation [19] that covalent intermetallics (e.g. TiAl) would exhibit smaller differ-ences between crystalline and atomic structure factors than ionic intermetallics (e.g. NiAl) is not supported by accurate calculations (see below).

The nature of the charge distribution in TiAl has recently received much interest from theoreticians [20–26], but no comparison has yet been made with experiment. Recently [19], Fox has determined seven structure factors of stoichiometric γ-TiAl using critical voltage electron diffraction measurements. His results were analyzed assuming (i) equal Debye–Waller factors for Al and Ti and (ii) that the structure factors can be represented by a superposition of spherically-symmetric densities about atomic sites. These results are reproduced in the first column of Table 1. The purposes of the present work are (i) to compare these precisely measured structure factors

with accurate theoretical calculations, (ii) to compare the ensuing experimental and theoretical Fourier-synthesized DEDD maps using the same Fourier truncation in both cases, (iii) to examine whether bonding effects are affected by higher order structure factors (currently outside the reach of experiment), and (iv) to contrast the bonding features of the covalent early transition metal aluminide TiAl with those of the more ionic, late transition metal aluminide NiAl.

2. MEASURED QUANTITIES AND THEIR ANALYSIS

We start by a summary of the measured (expt) quantities that will be compared below to their theoretical counterparts. We emphasize here the approximations involved in the data processing which ultimately limits accuracy of the ensuing DEDD maps.

The *dynamic* structure factor for momentum **G** is

$$F_{\text{expt}}(\mathbf{G}) = \sum_{\alpha=1}^{M} \rho_{\alpha}(\mathbf{G}) \, e^{i\mathbf{G}\cdot\tau_{\alpha}} \, e^{-\mathbf{G}\cdot\beta_{\alpha}\cdot\mathbf{G}} \qquad (1)$$

where $\rho_{\alpha}(\mathbf{G})$ is the Gth Fourier component of the charge density contributed by sublattice α (whose position vector in the unit cell is τ_{α}), and β_{α} is the anisotropic temperature coefficient tensor at site α, often approximated by the Debye–Waller factor $B_{\alpha}/16\pi^2$. Equation (1) represents (a universally used) *approximation* [13, 16] whereby temperatue effects are represented by smearing of the static structure factors

Table 1. Experimental and calculated static X-ray structure factors of γ-TiAl. We also list the structure factors corresponding to the superposition of free atoms (Ti[Ar]$3d^2 4s^2$ and Al[Ne]$3s^2 3p^1$) calculated using local density approximation (LDA) and relativistic Hartree–Fock (RHF) methods [28]

hkl	$\rho_{\text{expt}}(\mathbf{G})$	$\rho_{\text{calc}}(\mathbf{G})$	$\rho_{\text{expt}}(\mathbf{G}) - \rho_{\text{calc}}(\mathbf{G})$	$\rho_{\text{sup}}^{\text{LDA}}(\mathbf{G})$	$\rho_{\text{sup}}^{\text{RHF}}(\mathbf{G})$	$\rho_{\text{calc}}(\mathbf{G}) - \rho_{\text{sup}}^{\text{LDA}}(\mathbf{G})$
001	15.994 ± 0.065	16.058	− 0.064	15.818	15.831	0.240
110	14.166 ± 0.040	14.166	0.000	14.333	14.448	− 0.167
111	48.625 ± 0.055	48.625	0.000	48.954	49.052	− 0.329
002	46.198 ± 0.070	46.111	0.087	46.372	46.485	− 0.261
200	45.476 ± 0.070	45.476	0.000	45.961	46.073	− 0.485
201	11.282 ± 0.333	11.200	0.082	11.284	11.302	− 0.084
112	> 10.064	10.686		10.591	10.585	0.095
202		38.436		38.449	38.506	− 0.013
220	38.364	38.363	0.001	38.211	38.267	0.152
003		8.932		8.926	8.865	0.006
221		8.790		8.782	8.716	0.008
310		8.215		8.360	8.278	− 0.145
113		34.771		34.705	34.738	0.066
311		34.311		34.342	34.374	− 0.031
222		33.470		33.378	33.404	0.092
203		7.526		7.580	7.465	− 0.054
312		7.257		7.337	7.212	− 0.080
004		30.202		30.152	30.163	0.050
400		29.523		29.663	29.673	− 0.140
223		6.953		6.955	6.822	− 0.002
401		6.757		6.925	6.792	− 0.168
114		6.869		6.889	6.757	− 0.020
330		6.934		6.841	6.710	0.093
313		27.841		27.835	27.842	0.006
331		27.773		27.639	27.645	0.134
204		27.414		27.390	27.396	0.024
402		27.032		27.111	27.118	− 0.079
420		27.066		27.020	27.027	0.046
421		6.705		6.700	6.586	0.005
332		6.744		6.680	6.572	0.064

Units are electron/cell, where the tetragonal cell contains four atoms (twice the two atoms primitive unit cell). $\rho(\mathbf{G} = 0) = 70$.

about equilibrium atomic sites. This factorization will be used here.

The *dynamic* real-space charge density can be synthesized from the Fourier components of equation (1) by summing them up to a maximum momentum G_{max} available from diffraction experiments. This gives the real space "dynamic" charge density

$$F_{expt}(\mathbf{r}, \mathbf{G}_{max}) = \sum_{\mathbf{G}}^{\mathbf{G}_{max}} F_{expt}(\mathbf{G}) \, e^{i\mathbf{G}\cdot\mathbf{r}} \qquad (2)$$

where the result naturally depends on the highest momentum ($\mathbf{G}_{max}$) included in this sum. In the case of TiAl, the Debye–Waller factor of Ti and Al have been assumed [19] to be equal ($\langle B \rangle = B_{Ti} = B_{Al}$). In this case one can simply extract the *static* (purely electronic) structure factor through

$$\rho_{expt}(\mathbf{G}) = F_{expt}(\mathbf{G}) \, e^{\langle B \rangle G^2 / 16\pi^2}. \qquad (3)$$

(Note that we consistently denote dynamic and static quantities as F and ρ, respectively.)

It is important to realize that $\rho_{expt}(\mathbf{G})$ is not a purely experimental quantitiy. It is determined in an iterative refinement process [18(a), (b)] in which a given (approximate) theoretical model is used to adjust $\rho_{expt}(\mathbf{G})$. The most widely used approach (employed, among others, for NiAl [6] and TiAl [19]) is to assume that $\rho_\alpha(\mathbf{G})$ of equation (1) is the Fourier transform of a *spherically-symmetric* charge density $\tilde{\rho}_\alpha(\mathbf{r})$ centered about α. One further assumes that this density can be approximated by the calculated spherical density of the free atoms. In this case (absorbing the constant $16\pi^2$ into B), the structure factors of the $L1_0$ structure are

The *dynamic* real-space charge density can be angular momentum (l) harmonic series

$$\rho_\alpha(\mathbf{r}) = \sum_{l=0}^{\infty} R_l(r) K_l^{\gamma_1}(\hat{r}) \qquad (5)$$

where r and $\hat{r}$ are the modulus and direction of $\mathbf{r}$ (about τ_α), respectively, $K_l^{\gamma_1}(\hat{r})$ is the lattice harmonics belonging to the totally-symmetric (a_1) representation of the αth site group, and $R_l(r)$ are the αth site radial functions [defined by the convolution of $\rho_\alpha(\mathbf{r})$ with $K_l^{\gamma_1}(\hat{r})$]. In the $L1_0$ structure of TiAl, the symmetry-allowed l values are $0, 2, 4, 6, 8 \ldots$. The *conventional data refinement technique* [6, 18, 19] (used also for NiAl [6] and TiAl [19]) *retains only the $l = 0$ term in the general expansion* [equation (5)]. It is within this approximate model that internal consistency (i.e. the R-factor) is examined. The error associated with neglecting the $l \neq 0$ components is thus difficult to determine. More elaborate methods [5, 12, 13, 16, 17] use a few nonzero l values. There one assumes some functional form for $R_l(r)$ and fits its parameters to a few measured structure factors. Equation (5) is then used to (extrapolatively) calculate *any* $\rho(\mathbf{G})$.

Once $\rho_{expt}(\mathbf{G})$ is determined, it can be used to synthesize, in analogy with (2), the *static* real space electronic charge density

$$\rho_{expt}(\mathbf{r}, \mathbf{G}_{max}) = \sum_{\mathbf{G}}^{\mathbf{G}_{max}} \rho_{expt}(\mathbf{G}) \, e^{i\mathbf{G}\cdot\mathbf{r}}. \qquad (6)$$

As has been recognized many times previously (e.g. see Refs [11–14] and [18(b)]) the Fourier series of the *total* charge density of equations (2) and (6)

$$F_{expt}(\mathbf{G}) = \begin{cases} \tilde{\rho}_{Ti}(\mathbf{G}) \, e^{-B_{Ti}G^2} + \tilde{\rho}_{Al}(\mathbf{G}) \, e^{-B_{Al}G^2}; & (hkl) \text{ are all even or all odd} \\ \tilde{\rho}_{Ti}(\mathbf{G}) \, e^{-B_{Ti}G^2} - \tilde{\rho}_{Al}(\mathbf{G}) \, e^{-B_{Al}G^2}; & (hkl) \text{ are mixed even and odd and } h+k = \text{even} \qquad (4) \\ 0; & (hkl) \text{ are mixed even and odd and } h+k = \text{odd.} \end{cases}$$

The first line represents the f.c.c.-like "fundamental" reflections, while the second gives "superlattice" reflecions. When $\rho_{expt}(\mathbf{G})$ are determined from electron diffraction measurements made in a systematic row [19], one assumes that all unmeasured values $\rho(\mathbf{G} < \mathbf{G}_{max})$ are equal to the free-atom values of equation (4) computed with *spherical* densities. Through the refinement process, this affects the values of the measured values $\rho(\mathbf{G} \leqslant \mathbf{G}_{max})$. For example, in determining $\rho_{expt}(111)$ when only one electron diffraction measurement has been made in the (hhh) systematic row, one usually takes $\rho(222) = \tilde{\rho}_{atom}(222)$, and $\rho(333) = \tilde{\rho}_{atom}(333)$ etc. For the series $\mathbf{G} = (00h)$ Fox [19] determined $\rho_{expt}(001)$ and $\rho_{expt}(002)$ assuming $\rho_{expt}(003)$ and higher were given by $\tilde{\rho}_{atom}(333)$ etc. *In general, equation (4) with spherical densities is incorrect.* We know that $\rho_\alpha(\mathbf{r})$ [viz. equation (1)] must in fact have the symmetry of site α in the crystal rather than a spherical symmetry. The mathematically correct approach is to expand [13, 16] the Fourier transform of $\rho_\alpha(\mathbf{G})$ in a general

converges very slowly since the sharp features of $\rho(\mathbf{r})$ (associated with the rapid variation of the wavefunctions near the cores) give rise to many short-wavelength Fourier components. To overcome this difficulty it is possible to Fourier transform the *difference* between $\rho(\mathbf{r})$ and some model density $\rho_{model}(\mathbf{r})$ chosen such that its high Fourier components will approximately match those of $\rho(\mathbf{r})$. The focus is then on the static *deformation* electronic density distribution (DEDD)

$$\Delta\rho_{expt}(\mathbf{r}, \mathbf{G}_{max}) = \rho_{expt}(\mathbf{r}, \mathbf{G}_{max}) - \rho_{model}(\mathbf{r}, \mathbf{G}_{max}). \qquad (7)$$

The choices of ρ_{model} is obviously nonunique; a standard choice is to represent it as a superposition (sup) of calculated spherically-symmetric neutral atomic ground state charge densities $n_\alpha(\mathbf{r})$

$$\rho_{model}(\mathbf{G}) = \rho_{sup}(\mathbf{G}) = \sum_{\alpha=1}^{M} n_\alpha(\mathbf{G}) \, e^{-i\mathbf{G}\cdot\tau_\alpha} \qquad (8)$$

where $n_\alpha(\mathbf{G})$ is the Gth Fourier component of the free *atom* density $n_\alpha(\mathbf{r})$ [not to be confused with the *crystalline* quantity $\rho_\alpha(\mathbf{G})$ of equation (1)]. A variety of choices exist for $n_\alpha(\mathbf{r})$, e.g. relativistic Hartree–Fock calculations [27]†, local density data [28], configuration-interaction, etc. The corresponding "deformation electron density distribution" is then

$$\Delta\rho_{\text{expt}}(\mathbf{r}, \mathbf{G}) = \sum_{\mathbf{G}}^{\mathbf{G}_{\text{max}}} [\rho_{\text{expt}}(\mathbf{G}) - \rho_{\text{sup}}(\mathbf{G})] \, e^{i\mathbf{G}\cdot\mathbf{r}} \quad (9)$$

while the dynamic DEDD is thus

$$\Delta F_{\text{expt}}(\mathbf{r}, \mathbf{G}_{\text{max}}) = \sum_{\mathbf{G}}^{\mathbf{G}_{\text{max}}} [F_{\text{expt}}(\mathbf{G}) - F_{\text{sup}}(\mathbf{G})] \, e^{i\mathbf{G}\cdot\mathbf{r}}. \quad (10)$$

Previous studies on Si [12, 13] and NiAl [14] show that the overall features of the DEDD are not affected much by the incluson of the temperature factors, so either static or dynamic DEDD give a similar picture of the bonding. We will concentrate therefore on the static DEDDs.

3. CALCULATED QUANTITIES

While diffraction experiments produce discrete Fourier components of the charge density up to a finite (and often small) $\mathbf{G}_{\text{max}}$ value, electronic structure calculations for periodic crystals can produce the total static density $\rho_{\text{calc}}(\mathbf{r})$ directly in coordinate space, corresponding to Fourier series with $\mathbf{G}_{\text{max}} \to \infty$. This is obtained by summing the wavefunction-squared over all occupied band indices i and Brillouin zone wavevectors $\mathbf{k}$ enclosed within the Fermi energy ϵ_F

$$\rho_{\text{calc}}(\mathbf{r}, \mathbf{G}_{\text{max}} \to \infty) = \sum_{i, \mathbf{k}}^{\epsilon_F} N_i(\mathbf{k}) \psi_i^*(\mathbf{k}, \mathbf{r}) \psi_i(\mathbf{k}, \mathbf{r}) \quad (11)$$

where $N_i(\mathbf{k})$ is the occupation numbers of band i. Note that in such calculations no implication is made that ρ can be described by a superpositon of spherical objects. The Fourier components of the static density can then be computed as

$$\rho_{\text{calc}}(\mathbf{G}) = \frac{1}{\Omega} \int \rho_{\text{calc}}(\mathbf{r}) \, e^{-i\mathbf{G}\cdot\mathbf{r}} \, d\mathbf{r} \quad (12)$$

where Ω is the unit cell volume. This is the theoretical counterpart of equation (3). One can then synthesize a *truncated* DEDD by filtering out all Fourier components above a given momentum value of $\mathbf{G}_{\text{max}}$ as in equation (9). This provides the calculated DEDD

$$\Delta\rho_{\text{calc}}(\mathbf{r}, \mathbf{G}_{\text{max}}) = \sum_{\mathbf{G}}^{\mathbf{G}_{\text{max}}} [\rho_{\text{calc}}(\mathbf{G}) - \rho_{\text{sup}}(\mathbf{G})] \, e^{i\mathbf{G}\cdot\mathbf{r}}. \quad (13)$$

This is the theoretical counterpart of equation (9).

In Section 5.1 we will compare $\rho_{\text{expt}}(\mathbf{G})$ with $\rho_{\text{calc}}(\mathbf{G})$, while in Section 5.2 we will contrast $\Delta\rho_{\text{calc}}(\mathbf{r}, \mathbf{G}_{\text{max}})$ with $\Delta\rho_{\text{expt}}(\mathbf{r}, \mathbf{G}_{\text{max}})$. Section 6 examines Fourier truncation effects by calculating $\Delta\rho_{\text{calc}}(\mathbf{r}, \mathbf{G}_{\text{max}})$ as a function of $\mathbf{G}_{\text{max}}$. Section 7 compares the present calculation with previous theoretical results. Section 8 discusses the general features of the total, valence, and difference densities of TiAl, we also contrast the DEDD of TiAl with that of the hypothetical L1_0 structure of NiAl in Section 8.2. Finally, Section 9 provides a summary.

4. DETAILS OF CALCULATION

The single-particle wavefunctions $\{\psi_i(\mathbf{k}, \mathbf{r})\}$ of equation (11) are obtained by self-consistently solving the effective Schrödinger equation [7, 8] for a periodic TiAl solid in the L1_0 structure

$$\{-\tfrac{1}{2}\nabla^2 + V_{\text{e-ion}}(\mathbf{r}) + V_{\text{e-e,C}} + V_{\text{e-e,X}} + V_{\text{e-e,CR}}\}$$
$$\times \psi_i(\mathbf{k}, \mathbf{r}) = \epsilon_i(\mathbf{k}) \psi_i(\mathbf{k}, \mathbf{r}) \quad (14)$$

using the local density approximation [7, 8] (LDA). Here, $V_{\text{e-ion}}$ is the electron–ion Coulomb attraction, $V_{\text{e-e,C}}$ is the interelectronic (mean-field) Coulomb repulsion, $V_{\text{e-e,X}}$ is the average exchange interaction, $V_{\text{e-e,CR}}$ is the average correlation interaction and $\epsilon_i(\mathbf{k})$ are the band energies of band i at momentum $\mathbf{k}$. We use the local density description [7, 8] for $V_{\text{e-e,X}}$ and the correlation functional $V_{\text{e-e,CR}}$ of Ceperley and Alder [9], as parameterized by Perdew and Zunger [10]. Equation (14) was solved self-consistently by the linearized augmented plane wave (LAPW) method [29], in which: (i) core and valence electrons are included simultaneously (i.e. no pseudopotential approximation is used); (ii) no "shape approximations" to the potential or charge density are invoked. We expand the charge density and potential inside the αth muffin-tin spheres by lattice haromics up to angular momentum of $l = 8$, while the interstitial region is described by a plane wave expansion with kinetic energy cutoff of 57.0 Ry, core orbitals are treated self-consistently, retaining, however, only the spherically-symmetric part of their density; (iii) the electron–electron interactions are treated relativistically (using mass–velocity and Darwin terms [29]), except for spin-orbit effects which are neglected; (iv) a large basis set consisting of both real-space orbitals (inside the muffin-tin regions) and plane waves is used. The total number

---

†Doyle and Turner (Ref. [27]) were the first to calculate a decent set of relativistic-Hartree–Fock (RHF) free atom scattering factors for many elements and they also generated the interpolation coefficients. The latest set of such RHF scattering factors are compiled by E. N. Malsen, A. G. Fox and M. A. O'Keeffe [*International Tables for Crystallography*, Vol. C, p. 476 (edited by A. J. C. Wilson). Kluwer Academic, Dordrecht]. These are based on the Hartree–Fock calculation of Doyle and Turner [27] and D. T. Cromer and J. B. Mann [*Los Alamos Scientific Laboratory Report* LA-3816 (1968)] who used the RHF wavefunctions of M. A. Coulthard [*Proc. Phys. Soc.* **91**, 44 (1967)] and J. B. Mann (1968) {unpublished work reported in *International Tables of X-Ray Crystallography*, Vol. IV, p. 71. Kynoch, Birmingham (1974)].

of basis functions is ~140 per unit cell of 2 atoms. We find that increasing further the basis set beyond this or treating the core orbitals as nonspherical change the Fourier components $\rho(001)$, $\rho(110)$ and $\rho(111)$, by less than 0.1%. Our main approximation here is hence the use of the *local* density description of exchange and correlation [7, 8].

We have used the measured room-temperature lattice constants $a = 3.9985$ Å and $c = 4.0796$ Å of γ-TiAl [19]. The Brillouin zone sums of equation (11) were performed uisng 40 k-vectors in the irreducible section of the Brillouin zone. The muffin-tin radii used were $R_{Al} = T_{Ti} = 1.4023$ Å; the fraction of the unit cell volume spanned by the spheres is 70.84%.

The atomic charge densities $n_\alpha(\mathbf{r})$ for $\alpha = $ Al, Ti were calculated from an equation analogous to equation (14) but with free-atom, rather than periodic boundary conditions and a spin-unrestricted Hamiltonian (since Al and Ti are "open-shell" atoms). This Schrödinger equation was integrated numerically with high precision, so no basis functions were needed. In calculating the atomic densities n_α of equation (8) we used the observed† ground state configurations $[\text{Ne}]2s^2 2p^1$ for Al and $[\text{Ar}]3d^2 4s^2$ for Ti.

5. COMPARISON OF EXPERIMENT AND THEORY

5.1. The static structure factors $\rho(G)$

Table 1 lists the experimentally deduced [19] $\rho_{expt}(\mathbf{G})$ [equation (3)] and the calculated $\rho_{calc}(\mathbf{G})$ [equation (12)] static structure factors of γ-TiAl. We also give the structure factors $\rho_{sup}(\mathbf{G})$ [equation (8)] computed with the current LDA method as well as literature values [27] (see footnote on p. 3932) using the relativistic Hartree Fock (RHF) method. The experimental static structure factors were extracted [19] using an average Debye–Waller factor of $\langle B \rangle = 0.47 \pm 0.02$ Å^2 obtained by electron diffraction. In principle, for a binary ordered alloy system, the different atom types will have different Deybe–Waller factors designated B_{Ti} and B_{Al} in this case. However, calculations of the Debye–Waller factors for the different atom types for binary alloys using a classical nearest-neighbour atom approximation indicates that these are equal for temperatures near the Debye temperature [30] and for

NiAl, which has a Debye temperature of 402 K, $B_{Ni} = 0.51$ Å^2 and $B_{Al} = 0.49$ Å^2 at room temperature [31]. For TiAl, $\langle B \rangle = 0.47 \pm 0.02$ Å^2 at room temperature gives a Debye temperature of 452 ± 20 K which suggests that the difference between B_{Ti} and B_{Al} at room temperature will be less than the error 0.02 Å^2 on $\langle B \rangle$ and so the use of an average Debye–Waller factor to analyze the electron diffraction data would seem to be a very reasonable approximation. At low temperature, where quantum effects are important, B_{Al} will almost certainly be larger than B_{Ti} since Al has a lower relative atomic mass than Ti. Indeed, more recent electron diffraction work by Holmestad *et al.* [32] produced an average $\langle B \rangle$ for TiAl at 123 K of $\langle B \rangle = 0.275$ Å^2 with $B_{Ti} = 0.20$ Å^2 and $B_{Al} = 0.35$ Å^2 as the most likely values of the Debye–Waller factors for the individual atoms. $\langle B \rangle = 0.275$ Å^2 at 123 K corresponds to an average Debye temperature of 422 K and, although Holmestad *et al.* did not quote specific errors on their measured values of $\langle B \rangle$, B_{Ti}, and B_{Al}, their data indicates that the error on the Debye temperature derived from their $\langle B \rangle$ values shown above is at least ± 20 K. This means that they are in good agreement with the value of 452 ± 20 K adopted in the present work. Average Deybe–Waller factors have also been determined by powder X-ray diffraction [19] for both Ti–50 at.% Al and Ti–51 at.% Al and values of 0.57 ± 0.05 Å^2 and 0.66 ± 0.05 Å^2 respectively were obtained. Powder X-ray diffraction measurements of $\langle B \rangle$ in binary alloys are usually considered to be of poor accuracy because, in addition to the random errors shown, the systematic errors associated with the treatment of thermal diffuse scattering, anomalous dispersion, preferred orientation and extinction (if present) means that these measured values of B can be highly inaccurate. The good agreement between the independently measured values of B obtained by electron diffraction implies that the errors on the values obtained in this way are significantly smaller and thus much more acceptable for structure factor and charge density analyses.

Table 1 uses the normalization $\rho(000) = 2(Z_{Ti} + Z_{Al}) = 70$ electrons/cell, where the tetragonal cell contains four atoms (i.e. twice the two atom primitive unit cells). It is interesting to note that from Table 1 that the differences in $\rho_{sup}(\mathbf{G})$ calculated using the LDA or the RHF methods are fairly substantial: e.g. 115 millielectron for the (110) reflection. As G increases the difference remain constant for the superlattice reflections but diminishes for the fundamental reflections. Section 5.2 and Fig. 1 will examine the effects of these differences on the DEDD.

We noted from Table 1 the following:
(i) There is an excellent agreement between the $\rho_{expt}(\mathbf{G})$ and $\rho_{calc}(\mathbf{G})$ values (within 0.7%). The (002) reflection has the largest difference of 0.022 e/atom. The root mean square (rms) deviation is 0.013 e/atom. Similar level of agreement between

---

†The origin of this discrepancy between $\rho_{expt}(200)$ and $\rho_{calc}(200)$ for β-NiAl is unclear but Fox has recently carefully reappraised the $\rho_{expt}(200)$ value and the critical voltage experiments which led to the value of $\rho_{expt}(200)$ of Ref. [6] and it would seem that a combination of the approximate analysis method discussed in Section 2 [text surrounding equations (4) and (5)] and radiation damage disorder in lowering the measured (400) critical voltage, on which $\rho_{expt}(200)$ mostly depends, can fully account for this difference. Further electron diffraction experiments are planned to try and examine this hypothesis.

theory [14] and experiment [6] (0.7%) was also found for NiAl except for the (200) reflection where a larger error of 1.7% was found†.

(ii) The difference $\Delta\rho(\mathbf{G}) = \rho_{calc}(\mathbf{G}) - \rho_{sup}^{LDA}(\mathbf{G})$ [argument of equation (13)] gives the solid state bonding effects. These are seen to be substantial for the lower order reflections [e.g. 1.5, 1.2 and 1.1% for the (001), (110) and (200) reflections, respectively].

(iii) The bonding effects represented by the difference $\Delta\rho(\mathbf{G})$ are not negligible for $\mathbf{G}$ outside the measured range, e.g. $\Delta\rho(\mathbf{G})$ is 1.8% of $\rho_{calc}(\mathbf{G})$ for the (310) reflection. Other $\Delta\rho(\mathbf{G} > \mathbf{G}_{max})$ are smaller, but their accumulative effect is significant (see Section 6).

(iv) Contrary to initial expectations [19], the bonding effects $\Delta\rho(\mathbf{G})$ in the nominally more covalent TiAl are not *smaller* than in the nominally ionic NiAl. For example, in NiAl only for the (100) reflection does $\Delta\rho(\mathbf{G})$ exceeds 1%, while for TiAl it exceeds 1% for many reflections [e.g. (001), (110), (200) and (310)]. These large $\Delta\rho(\mathbf{G})$ values are thus not correlated with ionic vs covalent character but rather with the details of metal–metal d bonding (see Section 6).

We next compare the real-space DEDD $\Delta\rho_{expt}(\mathbf{r}, \mathbf{G}_{max})$ [equation (9)] with its theoretical counterpart $\Delta\rho_{calc}(\mathbf{r}, \mathbf{G}_{max})$ [equation (13)]. In both cases we restrict the sum in these equations to be the same $\mathbf{G}_{max}$ values (accessible to experiment). The effect of higher $\mathbf{G}$ values is examined in Section 6.

5.2. The deformation electron density distribution maps

We have assembled the DEDD [equation (9)] from the seven reflections (001), (110), (111), (002), (200), (201) and (220), whose structure factors are experimentally available [19]. Figure 1 compares the calculated and measured DEDD maps using the same LDA atomic reference density. It further examines the effect of using different atomic reference densities (LDA or RHF) on the resulting DEDD maps. These are depicted as contour plots in three planes: (i) the (010) plane exhibiting both Ti and Al atoms [(a), (d) and (g)], (ii) the (001) plane having only Al atoms [(b), (e) and (h)], and (iii) the (001) plane having only Ti atoms [(c), (f), and (i)]. Solid (dashed) contours give positive (negative) $\Delta\rho$ values. The left-hand side panels [(a)–(c)] show the calculated results using for ρ_{sup} the RHF atomic densities [equation (13)], the middle panels [(d)–(f)] show the calculated results using for ρ_{sup} the LDA atomic densities [equation (13)], while the right hand-side panels [(g)–(i)] show the experimental results using for ρ_{sup} the LDA atomic densities [equation (9)].

†The LDA atomic ground state for Ti is actually $[Ar]3d^34s^1$, which in this calculation is 0.1 eV below the experimentally observed $[Ar]3d^24s^2$ ground state configuration.

Comparisons of the left panels with the middle panels show the effects of the atomic reference density (LDA or RHF) on the resulting DEDDs. We see that these are rather similar (except for a slight difference in the magnitude). Hence, the Fourier-truncated DEDDs are qualitatively the same using either the LDA or the RHF atomic reference charge densities. However, the details of the *converged* DEDD maps using either the LDA or the RHF atomic reference charge densities are expected to be different since the corresponding $\rho_{sup}(\mathbf{G})$ values for the superlattice reflections show a substantial difference even for high $\mathbf{G}$ (see Table 1).

Comparison of the middle and the right panels of Fig. 1 gives difference between experiment and theory. It is apparent that if equally truncated, the DEDD maps $\Delta\rho_{calc}(\mathbf{r}, \mathbf{G}_{max})$ and $\Delta\rho_{expt}(\mathbf{r}, \mathbf{G}_{max})$ agree closely. We observe the following:

(i) Charge is lost from *atomic sites*: both Ti and Al lose electrons relative to the free atoms.

(ii) Charge accumulates in the *interstitial* regions (suggestive of both "covalent" and "metallic" bonding).

(iii) The Al DEDD in the (010) plane [Fig. 1(d)] exhibits an ellipsoidal shape with long axis parallel to the [100] direction. It also shows *accumulation* of charge along the [001] direction which is consistent with the polarization of p electrons.

(iv) The Ti (001) plane DEDD map shows nearly isotropic charge depletion about the atomic site [Fig. 1(f)]. This appears at first counter intuitive in that the electron distribution near Ti is expected to reflect the non-spherical $3d$ character. We will see below that this near spherical symmetry is an artifact fo Fourier truncation.

6. CONTRIBUTION OF STRUCTURE FACTORS WITH G OUTSIDE THE MEASURED RANGE

Lu *et al.* [14] have previously shown in the case of NiAl that the truncation of the Fourier series $\Delta\rho(\mathbf{r}, \mathbf{G}_{max})$ after the first few measured structure factors misses the directional d-like charge lobes near the Ni sites. Similar effects were noted in GaAs [11] and in Si [12, 13], even though in the latter case, a much larger set of accurately measured structure factors were available. We will next study how $\mathbf{G}_{max}$ affects the convergence of $\Delta\rho_{calc}(\mathbf{r}, \mathbf{G}_{max})$ for TiAl.

Figure 2(a)–(e) shows the calculated $\Delta\rho_{calc}(\mathbf{r}, \mathbf{G}_{max})$ in the all-Ti (001) plane as a function of the cutoff $\mathbf{G}_{max}$ (or equivalently the number N of symmetrized plane wave stars), while Fig. 2(f) gives the directly calculated $\Delta\rho_{calc}(\mathbf{r})$ [viz. equation (11)] without Fourier truncation (i.e. corresponding to $N \rightarrow \infty$ Fourier terms). The evolution with N of strong nonspherical character near the Ti sites is clearly evident. One needs to include $N \sim 20$ Fourier terms [corresponding to $\mathbf{G}_{max} = (400)$] to start seeing the directional bonding features of the Ti $3d$ electrons

$\Delta\rho(r, G_{max})$: restricted to the reflections
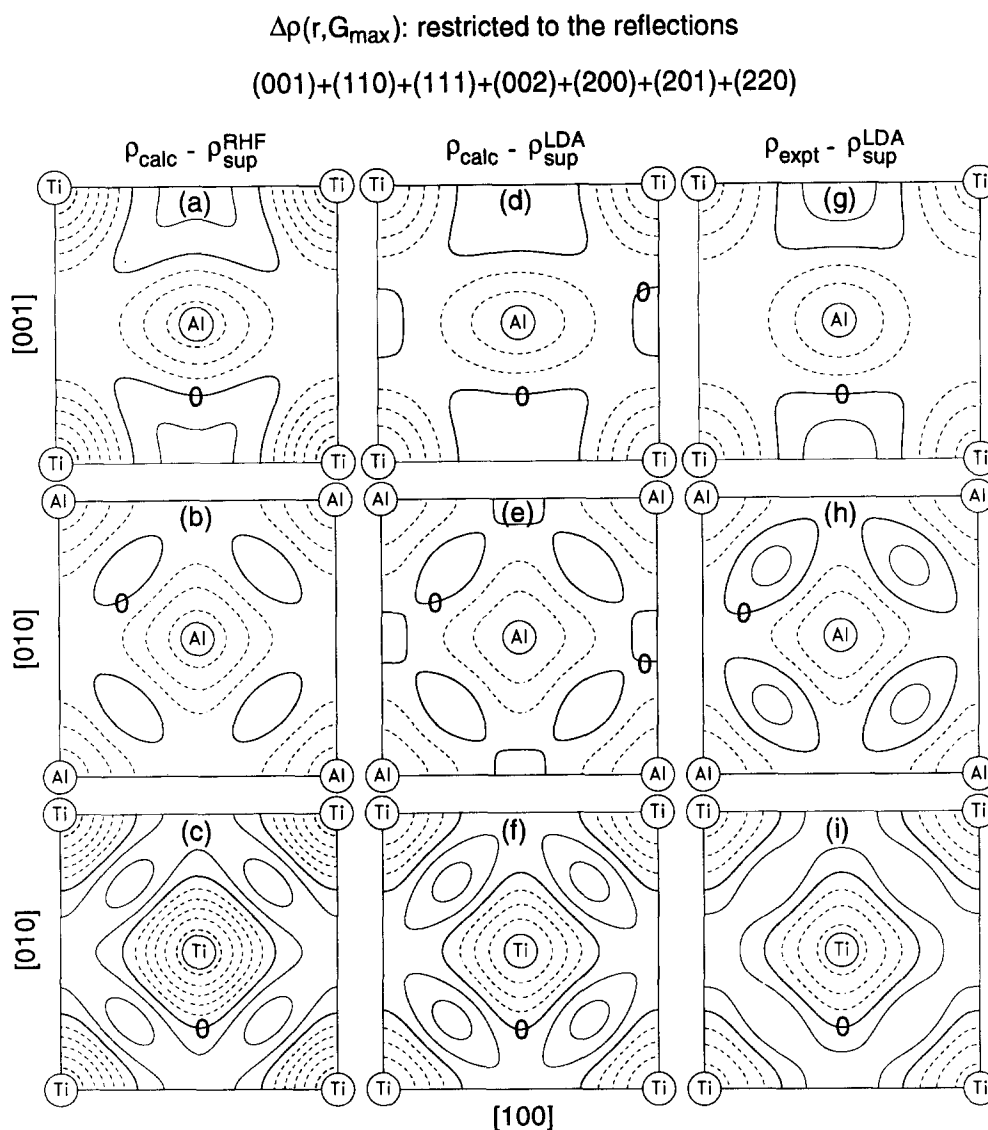
$(001)+(110)+(111)+(002)+(200)+(201)+(220)$

Fig. 1. Fourier truncated deformation electron density distribution maps $\Delta\rho(\mathbf{r}, \mathbf{G}_{max})$ for γ-TiAl. Here we include only structure factors at the G-values accessible experimentally. The left hand-side panels [(a)–(c)] show the calculated results subtracting the superposition of the relativistic-Hartree–Fock (RHF) atomic densities [equation (13)]. The middle panels [(d)–(f)] show the calculated results subtracting the superposition of the local density approximation (LDA) atomic densities [equation (13)], while the right hand-side panels [(g)–(i)] show the experimental results subtracting the superpositon of the LDA atomic densities [equation (9)]. We illustrate the bonding effects in three crystallographic planes: the mixed Ti and Al (010) plane [(a) and (d)], the all-Al (001) plane [(b) and (e)], and the all-Ti (001) plane [(c) and (f)]. The solid lines indicate charge accumulation, while the dashed lines indicate charge depletion. The thick lines next to a dashed line give the $\Delta\rho = 0$ contour as indicated by "0". The contour step is $0.02 \, e/\text{Å}^3$.

[Fig. 2(b)]. Observe how the elliptical interstitial DEDD at $N = 10$ [the feature labeled α in Fig. 2(a)] rotates its long elliptical axis for $N = 20$ [Fig. 2(b)] and that this feature dissociates into two spheres (labeled α and β) at $N = 30$ [Fig. 2(c)]. As N increases further the feature β moves gradually towards the Ti sites, developing a polarization towards the nearest neighbor Ti site. All of these features are absent if one limits G to the experimental available range. Using $N = 156$ terms we obtain a fairly well converged directional $3d$ bonds, however, the DEDD map is still rather noisy in the interstitial regions. This disappears as N is increased further [Fig. 2(f)].

To better appreciate the loss of information associated with truncating $\mathbf{G}_{max}$ to the experimentally accessible range, we show in Fig. 3 the calculated $\Delta\rho_{calc}(\mathbf{r}, \mathbf{G}_{max})$ as a surface plot for $N = 10$ [part (a)] and $N \to \infty$ [part (b)] [the latter corresponds to the contour plots of Fig. 2(a) and (f)]. This figure clearly reveals the absence [(a) $N = 10$] and existence [(b) $N \to \infty$] of complex directional charge accumulation and depletion in the Ti plane.

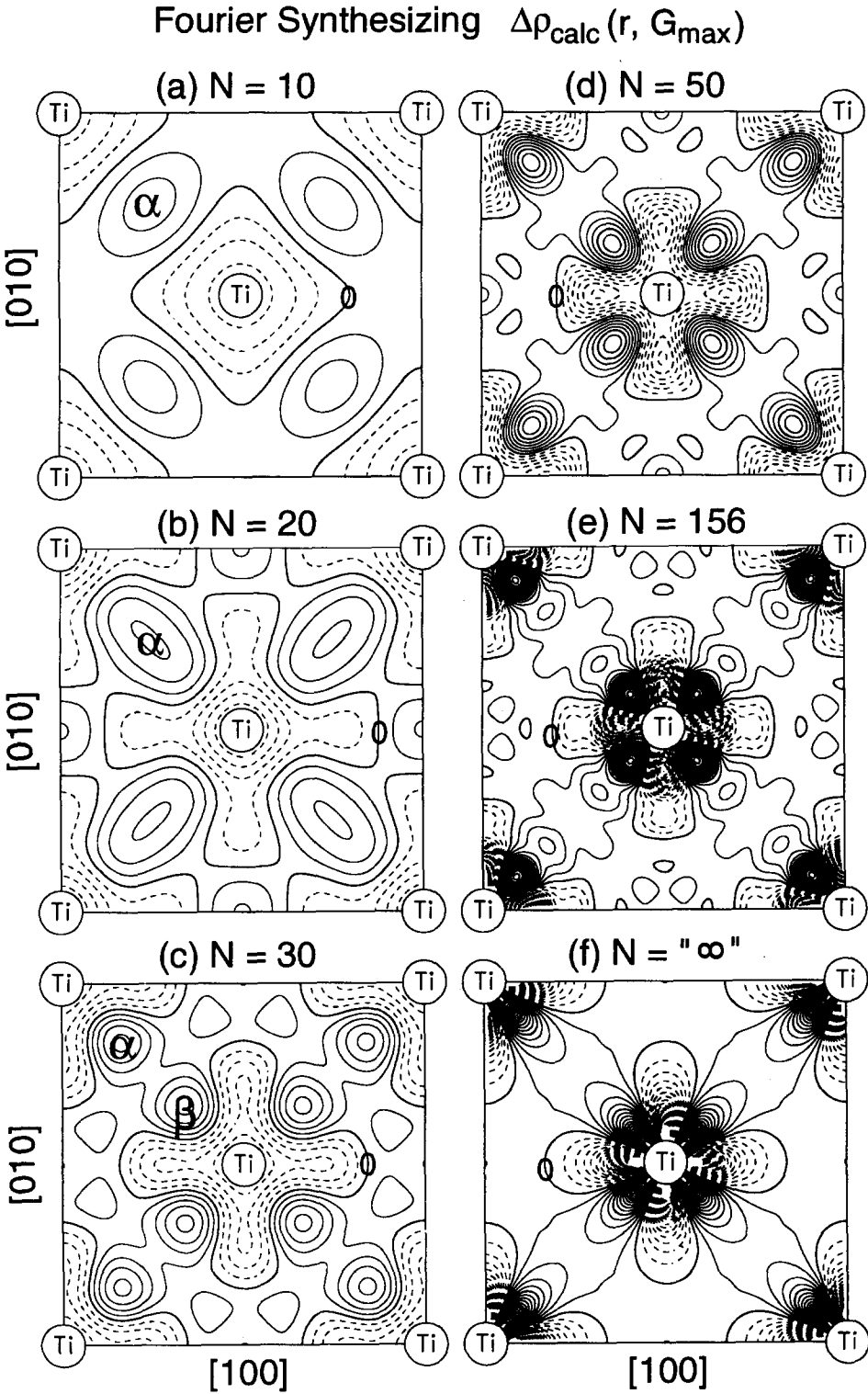## Fourier Synthesizing $\Delta\rho_{calc}(r, G_{max})$

Fig. 2. Calculated DEDD map $\Delta\rho_{calc}(\mathbf{r}, \mathbf{G}_{max})$ in the all-Ti (001) plane as a function of the cutoff $\mathbf{G}_{max}$ (or equivalently the number N of symmetrized plane wave stars). The solid lines indicate charge accumulation, while the dashed lines indicate charge depletion. The thick lines next to a dashed line give the $\Delta\rho = 0$ contour as indicated by "0". The contour step is 0.02 e/Å^3. The planes are defined in the caption to Fig. 1. Note how the features labeled α and β evolves as N increases.
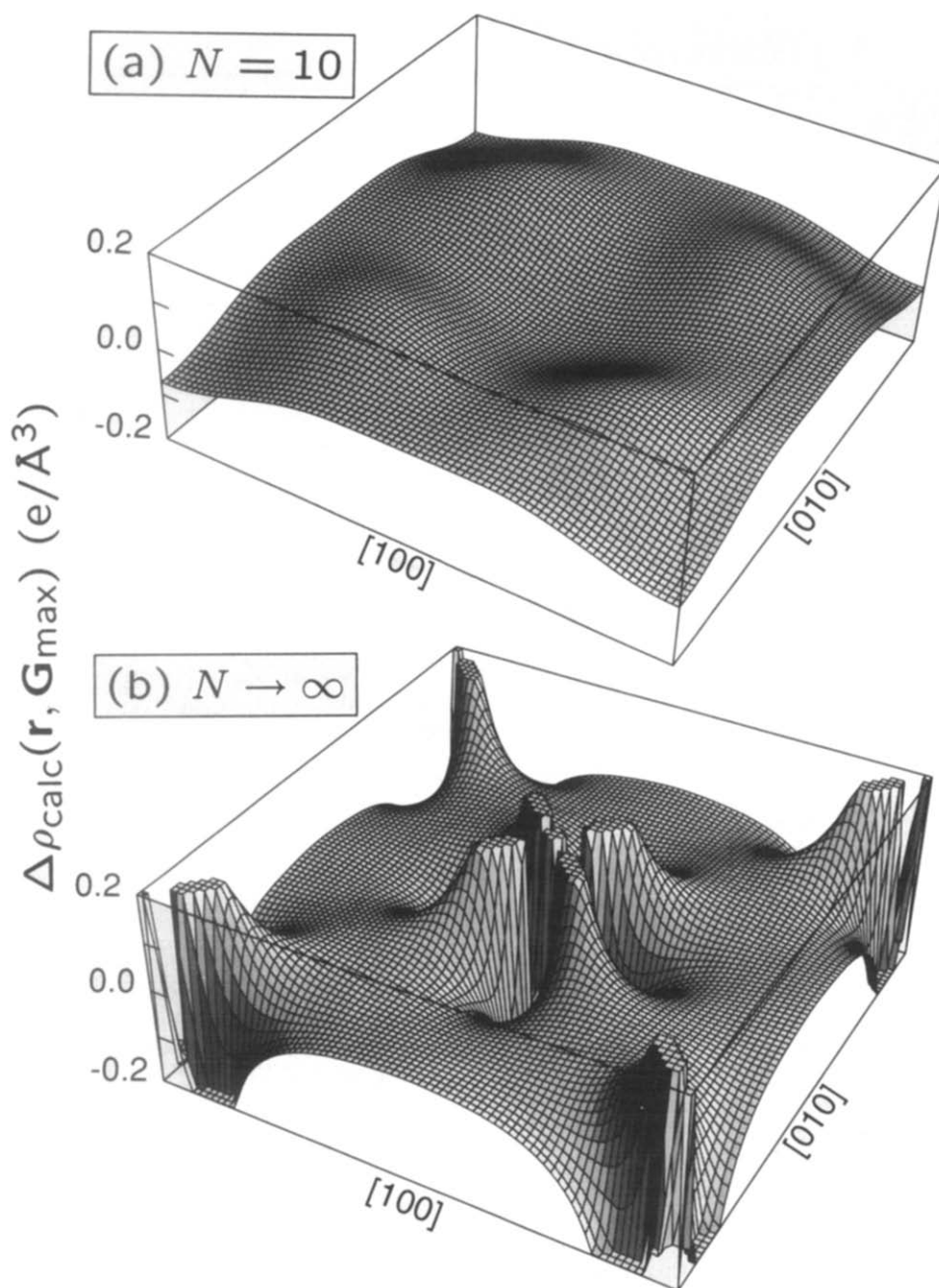
Fig. 3. Calculated DEDD map $\Delta\rho_{calc}(\mathbf{r}, \mathbf{G}_{max})$ in the (001) Ti plane shown here as a surface plot for Fourier truncation $N = 10$ (a) and $N \to \infty$ (b). These 3D plots correspond to the contour plots of Fig. 2(a) and (f), respectively. Ti atoms are located at the corners and at the center.

Clearly, the experimentally accessible momentum values gives a DEDD map which misses these important features; many more structure factors than currently experimentally available are needed to cure this problem.

The overall features of the DEDD are not affected much by the inclusion of the temperature factors. This was shown before on Si [12, 13] and NiAl [14], and is demonstrated again here for TiAl in Fig. 4. One notices that the calculated, static $\Delta\rho_{calc}(\mathbf{r}, \mathbf{G}_{max})$ [Fig. 4(a), $\mathbf{G}_{max} = (735)$ or $N = 156$ terms] and dynamic $\Delta F_{calc}(\mathbf{r}, \mathbf{G}_{max})$ [Fig. 4(b)] resemble each other.

Figure 5(a)–(c) shows the calculated *untruncated* DEDD of TiAl in (a) the mixed Ti–Al (010) plane, (b) the all-Al (001) plane and (c) the all-Ti (001) plane. Comparing this untruncated DEDD in Fig. 5(a)–(c) with the corresponding Fourier truncated DEDD in Fig. 1(d)–(f), we note the following:

(i) While the *truncated* DEDD in the mixed Ti–Al plane [Fig. 1(d)] captures roughly the main features of the untruncated DEDD [Fig. 5(a)], near the Ti atom, Fig. 1(d) misses the directional features of Fig. 5(a).
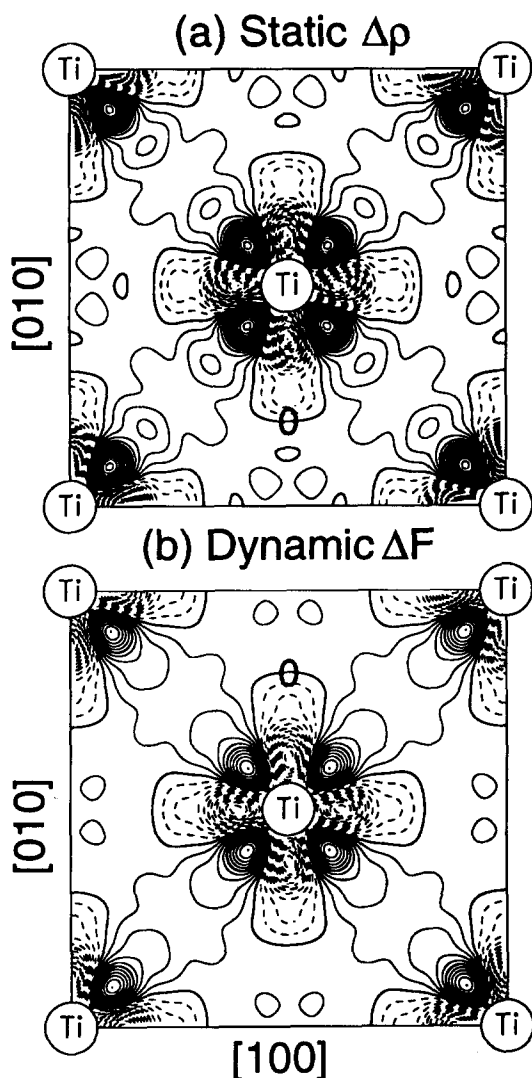
Fig. 4. Contour plots of the calculated (a) static $\Delta\rho_{calc}(\mathbf{r}, \mathbf{G}_{max})$ [equation (9)] and (b) dynamic $\Delta F_{calc}(\mathbf{r}, \mathbf{G}_{max})$ [equation (10)] deformation density in the all-Ti (001) plane of TiAl. $\mathbf{G}_{max} = (735)$ or $N = 156$ terms are included in the Fourier summation. The solid lines indicate charge accumulation, while the dashed lines indicate charge depletion. The thick lines next to a dashed line give the $\Delta\rho = 0$ contour as indicated by "0". The contour step is $0.02\, e/\text{Å}^3$.

(ii) In the (001) all-Al plane, Fig. 1(e) resembles Fig. 5(b) except for the magnitude.

Furthermore, the elliptical interstitial features found in the truncated series [Fig. 1(e)] disappear [Fig. 5(b)] upon converging the Fourier sum.

7. COMPARISON WITH PREVIOUS CALCULATIONS

There are a number of previous calculations concerning the electronic charge density in equiatomic TiAl [20–26]. None of these, however, gives calculated structure factors. Only three previous works have published valence, total, or DEDD maps: Ref. [23] displays the valence density, Ref. [24], gives

the DEDD, and Ref. [26] depicts the total charge density. Our calculated deformation, total and valence charge densities are given in Figs 5–8.

Anisimov et al. [20] calculated the electronic structure of TiAl using the linear combinations of muffin-tin orbitals (LMTO) method and found strong directional bonding between nearest-neighbour Ti atoms in the all-Ti (001) plane in agreement with the present work. Unfortunately they did not show the charge density contour plot. As a result of Anisimov et al.'s calculations, Greenberg et al. [21] suggested that because of the anisotropy of the charge density distribution around Ti atoms, the Peierls relief associated with dislocation motion is a many valleyed one in TiAl. In particular Greenberg et al. found that deep Peierls valleys could occur in directions such as $\langle 001]$, $\langle 110]$, and $\langle 113]$ which contain only Ti atoms. As a consequence they surmised that dislocations with their axes at right-angles to such directions could be sessile as a result of entrapment in deep Peierls valleys. Indeed, Court et al. [33] made detailed transmission electron microscope studies of dislocations in TiAl deformed at room temperature which appear to support this assertion since they indicated that slip systems which would be expected to dominate in TiAl, $\frac{1}{2}\langle 110]\{111\}$, were essentially sessile and suggested that this is the origin of low temperature brittleness in TiAl. Unfortunately it does not seem possible to confirm the anisotropy of the charge density around the Ti atoms in TiAl experimenally since very accurate measurements of many high-angle structure factors which have values very close to those of the free atom would be necessary to do this as indicated in Fig. 2. Consequently, only theoretical descriptions of the total charge density and the concept of Peierls many valley relief for this alloy currently seem possible.

Using the LAPW method, Chubb et al. [22] examined the charge density associated with the electronic states just below and above the Fermi energy. They found that the states immediately below Fermi energy exhibit strong bonding within the (001) all-Ti plane but weaker bonding between the Ti and Al layers (along the [001] direction). Total or valence density maps were not given so a direct comparison with our results is not possible.

Fu and coworkers [23, 24] have also calculated the elastic constants of TiAl using the LAPW melthod finding $C_{44}/C_{66} = 2.4$. They attribute this large anisotropy to enhanced bonding between Ti (001) layers and the Al (001) layers. However, this large C_{44}/C_{66} ratio was not reproduced by Mehl et al. [34] who have calculated the elastic constants of TiAl using an independent LAPW program: Mehl et al.'s other C_{ij} values are within 7% of those calculated by Fu and Yoo [23], but the C_{66} value was exactly twice as large as that of Fu and Yoo (the C_{44}/C_{66} value of Mehl et al. is 1.26 while that of Fu and Yoo's is 2.4). This discrepancy should be resolved by examining these particular calculations (one must be in error).

Woodward *et al.* [25] determined the electronic structure of planar faults in TiAl using the muffin-tin (MT) layered Korringa–Kohn–Rostoker (MT-LKKR) method. These authors presented electronic charge density maps associated with the electronic states in two different energy windows below the Fermi energy. They noticed directional d_{xy} bonding in the (001) Ti plane and polarization of Al-p
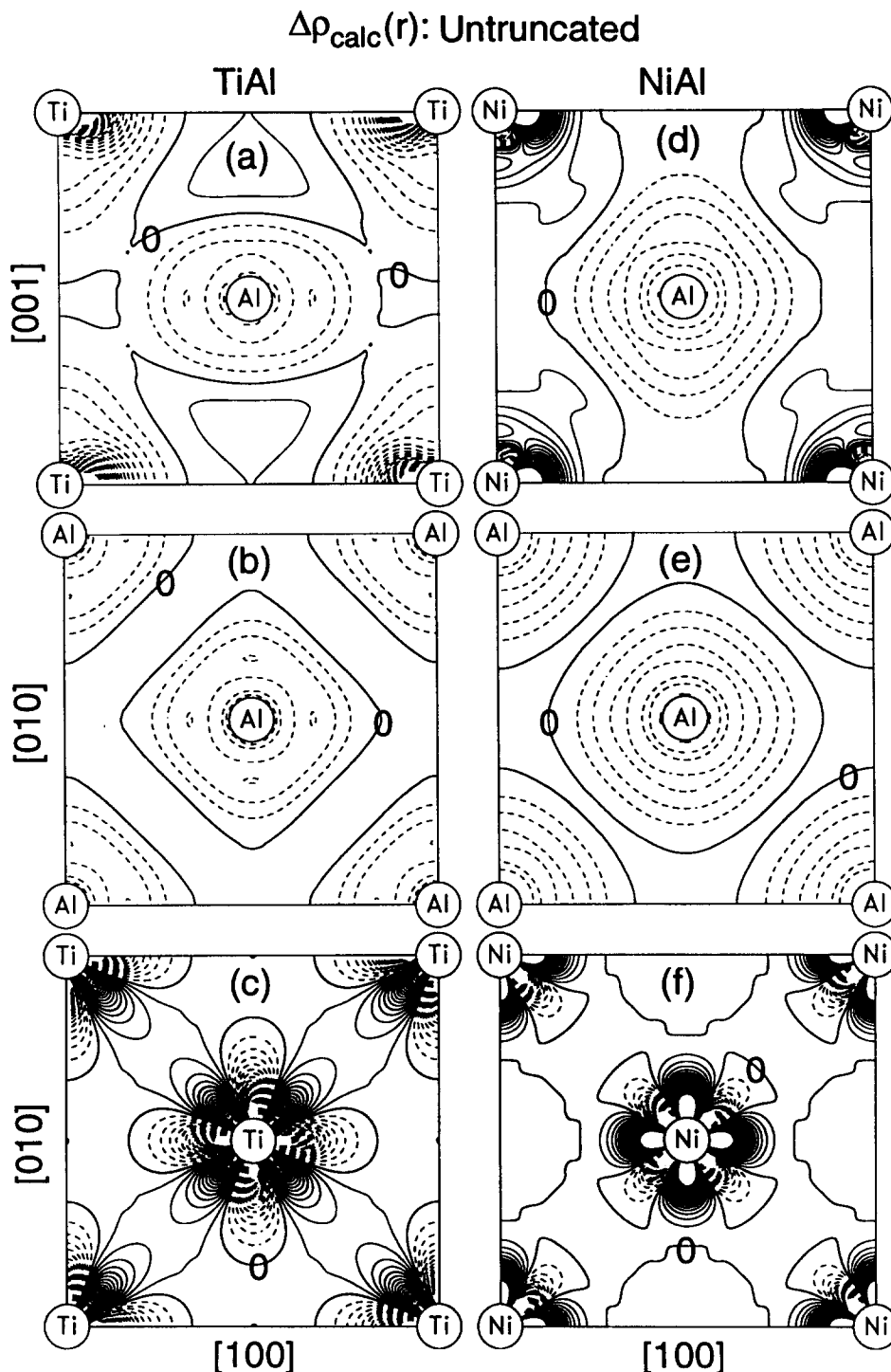
$\Delta\rho_{calc}(r)$: Untruncated

Fig. 5. Calculated untruncated DEDD maps $\Delta\rho_{calc}(r)$ for TiAl (left panels) and NiAl in a hypothetical $L1_0$ structure (right panels) in three planes: the mixed (010) Ti–Al and Ni–Al plane [(a) and (d)], the all-Al (001) plane [(b) and (e)], and the (001) Ti or Ni plane [(c) and (f)]. The solid lines indicate charge accumulation, while the dashed lines indicate charge depletion. The thick lines next to a dashed line give the $\Delta\rho = 0$ contour as indicated by "0". The contour step is $0.02\,e/Å^3$. The lattice parameters are $a = 3.9985\,Å$ and $c = 4.0796\,Å$ for TiAl and $a = c = 3.6366\,Å$ for NiAl.
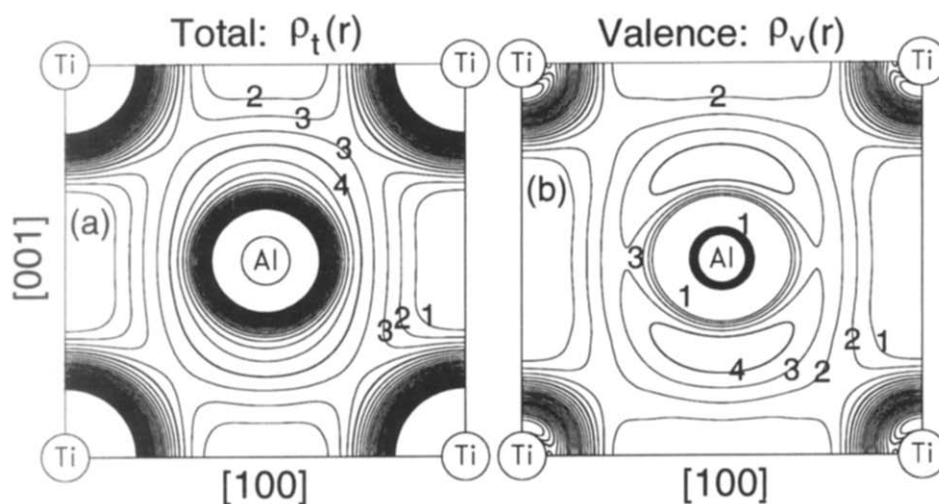
Fig. 6. Calcualted (a) total density $\rho_t(\mathbf{r})$ and (b) valence density $\rho_v(\mathbf{r})$ for TiAl in the (010) Ti–Al plane. The contours in this plot are spaced logarithmically: the successive contour values differ by $\rho_{n+1}/\rho_n = 1.105$. The contours with the label "1" have a value of $0.15\,e/\text{Å}^3$.

states along the [001] direction. These features were also observed by Fu *et al.* [23, 24] in their LAPW calculations. Their calculated valence charge density [23] and deformation charge density [24] are very similar to the present results of Figs 5 and 6 respectively.

More recently, Eberhart *et al.* [26] attempted to associate ductility and brittleness with topological

features in the electronic charge density, i.e. with critical points in the charge density. The calculations were done using the MT-LKKR method. As an example, they speculate that the brittleness (ductility) of TiAl (CuAu) in the L1$_0$ structure correlates with the presence (absence) of the complex topology of minima and various saddle points in the total charge density of TiAl (CuAu). For TiAl, they found in their
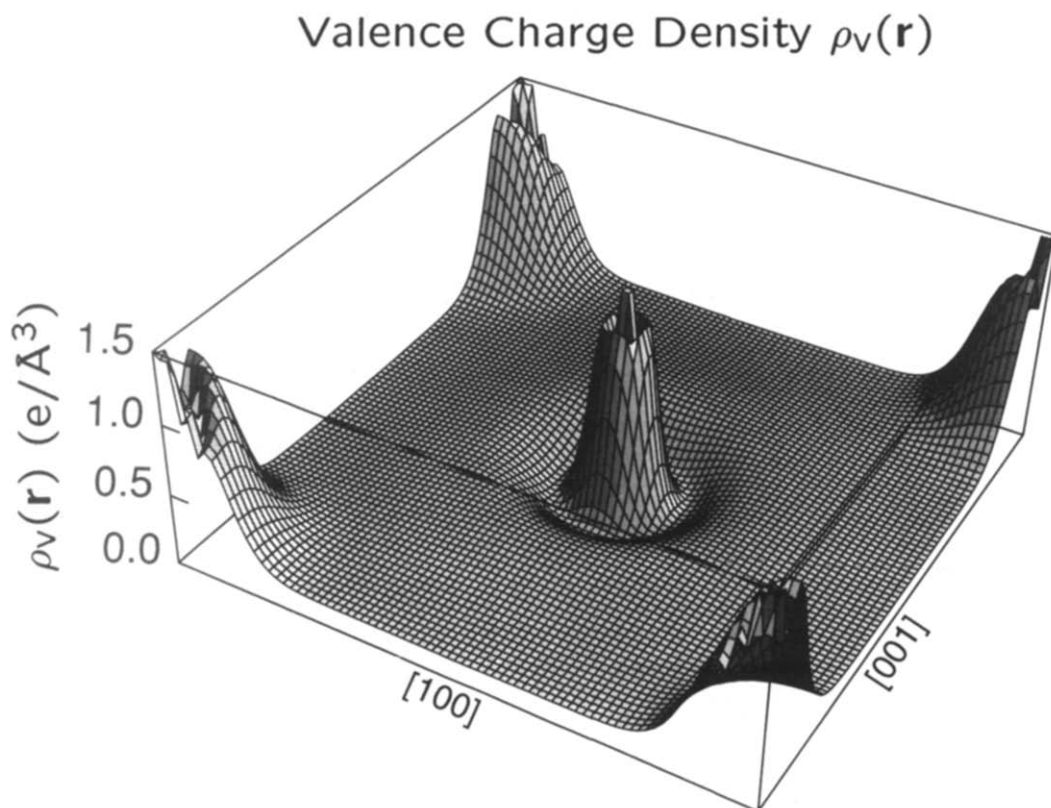

Fig. 7. Calculated valence charge density in the mixed Ti and Al (010) plane viewed as a surface plot. This plot clearly shows ridges and valleys near the atomic sites as well as the absence of minimums and saddle points along the [100] Ti–Ti and [001] Ti–Ti bond directions.
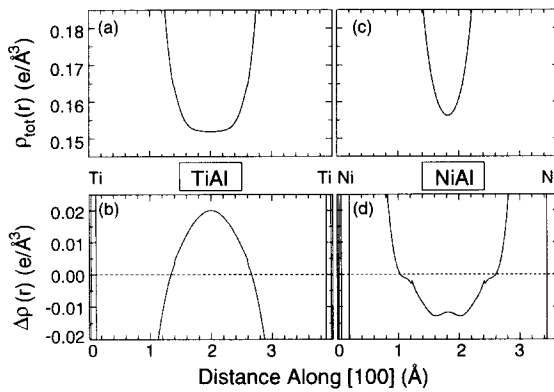
Fig. 8. Calculated total charge densities (top panels) and DEDD (bottom panels) for $L1_0$ TiAl and $L1_0$ NiAl along the [100] bond directions.

MT-LKKR calculation a double minimum in ρ_{tot} along the Ti–Ti [001] and [100] directions. We have carefully repeated these calculations, using our LAPW method which does not involve the muffin-tin approximation. All convergence parameters were increased so the errors in the interstitial charge density were below 0.0004 e/Å^3. We arrived at this estimated accuracy by varying: (i) number of Brillouin zone k-points used in sampling the density; (ii) the highest angular momenta l_{max} used in the lattice harmonics expansion; (iii) the average number of LAPW basis function used in wavefunction expansion; (iv) the number of symmetrized star functions used to expand the charge density and potential in the interstitial region; and (v) treating Ti 3s and 3p as core states or as non-spherical band states. Our results are depicted in Fig. 8. We see that the double minimum along the Ti–Ti [100] direction found by Eberhart et al. [26] using the MT-LKKR method are absent in the presently calculated total density [Fig. 6(a) and Fig. 8(a)] or valence density [Fig. 6(b) and Fig. 7] or the DEDD [Fig. 5 and 8(b)]. These features are also absent from the valence charge density of Fu and Yoo [23] (which closely resembles the total charge density in the interstitial regions). Our results for ρ_{tot} reveals no double minimum also along the Ti–Ti [001]. These considerations suggest that the complex topology of minima and saddle points found by Eberhart et al. might reflect an artifact of the MT-LKKR method, and thus does not provide a correct description of the ductility (or lack of it) in $L1_0$ CuAu (TiAl).

It appears that at present there is no well-established relationship between the electronic charge density in TiAl and its mechanical properties.

8. BONDING IN TiAl

8.1. Total and valence charge density in TiAl

In this section we use the calculated untruncated charge densities to study the bonding features in TiAl.

Figure 6(a) shows the total charge density of γ-TiAl in the (010) Ti–Al plane as a contour plot with logarithmic increments. Here we include in equation (11) all bands i starting from 1s, and no charge difference is taken. One notices the following: (i) the outer contours around the Al site have an elliptic shape directed along the [001] (p_z-like polarization). (ii) Charge is distributed nearly uniformly in the interstitial areas indicating "metallic" bonding. (iii) The nearly spherical charge density contours near the atomic sites for both Ti and Al reflect the chemically inert core electrons (1s, 2s, 2p for Al and 1s, 2s, 2p, 3s, 3p for Ti). These core states play a relatively minor role in forming the solid.

To see the effects of the bonding electrons, we depict in Fig. 6(b) the valence charge density [in the (010) Ti–Al plane] obtained by restricting the sum in equation (11) to bands above the Al 2p and Ti 3p. One observes a nearly uniform distribution of interstitial charge and elliptical contours around the Al site. Furthermore, one notices that there are local lobes and valleys inside the ellipsoid near Al site and that near the Ti site there is a lobe pointing towards the next nearest-neighbor Ti along the [001] direction. These features can be viewed better by a three-dimensional surface plot shown in Fig. 7. This figure clearly shows that the valence charge density (i) is nearly uniform between the atoms, (ii) it exhibits directional bonding near the Ti sites, and (iii) it has peaks and valleys near the atomic sites.

The overall bonding patterns in γ-TiAl can be explained in terms of orbitals as follows: bonding arises from the non-spherical depletion of electrons from both Al and Ti atomic sites with redistribution such that there is considerable build-up of electrons in $\langle 110 \rangle$ directions between nearest-neighbor Ti atoms in all-Ti (001) planes. This is consistent with overlap of d_{xy} orbitals (in this notation $x = [100]$, $y = [010]$ and $z = [001]$). There is a much smaller build-up of electrons between second nearest-neighbor Ti atoms in the all-Ti (001) planes which appears to arise from d^4p^2 hybrid orbitals occurring as a result of the polarization of the Al p_z state along [001] discussed above. There is also a very small build-up of charge between third nearest-neighbor Ti atoms along [001] consistent with the overlap of $d_{2z^2 - x^2 - y^2}$ orbitals. The bonding between nearest-neighbor Al atoms in all-Al (001) planes appears to be simply metallic.

8.2. TiAl vs NiAl

While TiAl crystallizes in the f.c.c.-type $L1_0$ structure, NiAl crystallizes in the b.c.c.-like B2 (CsCl) structure. The electronic structure of NiAl in its equilibrium B2 strucrure was previously discussed by Lu et al. [14]. To compare bonding trends, we contrasted here the DEDD maps of TiAl with that of NiAl in an hypothetical $L1_0$ structure. We use the lattice parameters $a = c = 3.6366$ Å, thus conserving the unit cell volume of the B2 structure. The TiAl

lattice constants are roughly 9.4% *larger* than that of NiAl. This reflects the fact that Ni has a nearly full (more localized) d shell (atomic configuration $[Ar]3d^84s^2$), so its nuclear charge is better screened by the d shell relative to Ti. Figure 5(d)–(f) gives contour plots of the DEDD, while Fig. 8(c) gives the total density. Considering first the *total* density, we see similar features in TiAl [Fig. 8(a)] and NiAl [Fig. 8(c)]. Also, considering the DEDD maps (Fig. 5) we see that in the mixed transition metal–Al plane [parts (a) and (d) of Fig. 5] and in the Al plane [parts (b) and (e) of Fig. 5] the DEDD of NiAl and TiAl are practically similar. However, the transition metal plane [parts (c) and (f) of Fig. 5] show significant differences in the DEDD: In TiAl the t_{2g}-like (d_{xy}) lobes pointing *towards* the nearest Ti sites are *positive* and the e_{2g}-like ($d_{x^2-y^2}$) lobes pointing in *between* the nearest Ti sites [towards the next nearest (NN) Ti along [100] and [010]] are *negative*. In NiAl the situation is reversed. This qualitative difference in the DEDD between the next nearest neighbor transition atoms can be seen more clearly in the line plot of Fig. 8(b) and (d): while in TiAl there is a *depletion* of charge in the region $0.2 \text{ Å} < r < 1.0 \text{ Å}$, in NiAl there is charge *accumulation* there. Furthermore, in the interstitial region ($r \sim 2 \text{ Å}$) there is charge *accumulation* in TiAl but *depletion* in NiAl. Note that while the total charge density [Fig. 8(a) and (c)] exhibit local minima in the midpoint between the transition metal atoms for TiAl and NiAl, the DEDD exhibits a local maximum for TiAl but a local minimum (with a small bump) for NiAl. This qualitatively different DEDD can be understood by examining the densities of states of these compounds (Refs [22, 35]): The Fermi energy in TiAl is located in the $3d$ bonding region, so the charge density below the Fermi energy exhibits the strong Ti–Ti $3d$ directional bonding directed towards the nearest-neighbor [22]. In contrast, the Fermi energy in [35] NiAl (in either the B2 or the hypothetical $L1_0$ structures), is located *above* the $3d$ bonding peaks, so the anti-bonding states are occupied. Thus the charge density lobes are not directed towards nearest neighbors as in TiAl. Instead they are directed towards the *next* nearest-neigbors. This tendency of charge accumulation directed towards the next nearest neighbors in NiAl was also noted by Schultz and Davenport [36].

9. SUMMARY AND CONCLUSION

We find:

(i) Excellent agreement between the calculated $\rho_{calc}(G)$ and measured $\rho_{expt}(G)$ structure factors (within 0.7%). The r.m.s. error is 0.013 e/atom, while maximum error is 0.022 e/atom.

(ii) By restricting the Fourier sum to the experimentally accessible G values, the Fourier truncated DEDD maps $\Delta\rho_{calc}(r, G_{max})$ and $\Delta\rho_{expt}(r, G_{max})$ resemble closely each other. The truncated DEDD maps are insensitive to the use of RHF or LDA reference atomic superpositon charge densities.

(iii) While the *truncated* DEDD in the mixed Ti–Al plane captures roughly the main feature of the full DEDD, in the Ti-layer, truncated DEDD completely misses the directional features of the full DEDD. Many more structure factors than currently accessible will be needed to observe directional d bonding in measured DEDD maps.

(iv) The presently calculated valence charge density and DEDD are in good agreement with previous calculation of Fu *et al.* [23, 24]. However, our total charge density map differs substantially from that of Eberhart *et al.* [26]. Their arguments on the relationship between brittleness/ductility and the topological features of the charge density are not supported by our calculation.

(v) The main bonding features in TiAl can be described as (a) non-spherical charge depletion from both Al and Ti atomic sites (recall that in B2 NiAl, the Ni atom gains charge while Al loses charge [14]), (b) redistribution of charge such that there is considerable build-up of electrons between nearest-neighbor Ti atoms in all-Ti (001) planes, (c) a smaller charge build-up between second nearest-neighbour Al atoms in all-Al (001) planes is simply metallic.

(vi) While TiAl exhibit strong nearest-neighbor bonding in the Ti plane, the hypothetical $L1_0$ form of NiAl has strong bonding in the *second* nearest-neighbor Ni plane. Indeed, TiAl shows a charge depletion near the atomic sites in the [100] direction, while NiAl exhibits charge accumulation there.

REFERENCES

1. F. K. Larsen and N. K. Hansen, *Acta crystallogr. B* **40**, 169 (1984).
2. A. G. Fox, M. A. Tabbernor and R. M. Fisher, *J. Phys. Chem. Solids* **51**, 1323 (1990).
3. J. M. Zuo, J. C. H. Spence and M. O'Keeffe, *Phys. Rev. Lett.* **61**, 353 (1988).
4. P. J. E. Aldred and M. Hart, *Proc. R. Soc. A* **332**, 223 (1973); S. Cummings and M. Hart, *Aust. J. Phys.* **41**, 423 (1988).
5. M. Deutsch, *Phys. Lett. A* **153**, 368 (1991); *Phys. Rev. B* **45**, 646 (1992); see also **46**, 607E (1992).
6. A. G. Fox and M. A. Tabbernor, *Acta metall. mater.* **39**, 669 (1991).
7. P. Hohenberg and W. Kohn, *Phys. Rev.* **136**, B864 (1964).
8. W. Kohn and L. J. Sham, *Phys. Rev.* **140**, A1133 (1965).
9. D. M. Ceperley and B. J. Alder, *Phys. Rev. Lett.* **45**, 566 (1980).

10. J. P. Perdew and A. Zunger, *Phys. Rev. B* **23**, 5048 (1981).
11. J. E. Bernard and A. Zunger, *Phys. Rev. Lett.* **62**, 2328 (1989).
12. Z. W. Lu and A. Zunger, *Acta crystallogr. A* **48**, 545 (1992).
13. Z. W. Lu, A. Zunger and M. Deutsch, *Phys. Rev. B* **47**, 9385 (1993).
14. Z. W. Lu, S.-H. Wei and A. Zunger, *Acta metall. mater.* **40**, 2155 (1992).
15. J. M. Zuo, J. C. Spence and M. O'Keeffe, *Phys. Rev. Lett.* **62**, 2329 (1989).
16. B. Dawson, *Proc. R. Soc. Lond. A.* **298**, 264 (1967); *ibid.* **298**, 379 (1967).
17. M. A. Spackman, *Acta crystallogr. A* **42**, 469 (1986).
18. (a) P. J. Coppens and P. J. Becker, in *International Tables for Crystallography*, Vol. C (edited by A. J. C. Wilson), p. 627. Kluwer, Dordrecht (1992). (b) D. J. Smart and C. J. Humphreys, in *Inst. Phys. Conf. Ser.* (edited by P. J. Dobson, J. B. Pendrey and C. J. Humpreys), Vol. 41, p. 145 (1978).
19. A. G. Fox, *Phil. Mag. Lett.* **68**, 29 (1993).
20. V. I. Anisimov, G. V. Ganin, V. R. Galakhov and E. Z. Kurmayev, *Phys. Met. Metall.* **63**, 192 (1987).
21. B. F. Greenberg, V. I. Anisimov, Y. N. Gornostirev, and G. G. Taluts, *Scripta metall.* **22**, 859 (1988).
22. S. R. Chubb, D. A. Papaconstantopoulos and B. M. Klein, *Phys. Rev. B* **38**, 12120 (1988).
23. C. L. Fu and M. H. Yoo, *Phil. Mag. Lett.* **62**, 159 (1990); *Mater. Res. Soc. Symp. Proc.* **186**, 265 (1991).
24. C. L. Fu, Y.-Y. Ye and M. H. Yoo, *Mater. Res. Soc. Symp. Proc.* **288**, 21 (1993).
25. C. Woodward, J. M. MacLaren and S. Rao, *Mater. Res. Soc. Symp. Proc.* **213**, (1991); *J. Mater. Res.* **7**, 1735 (1992).
26. M. E. Eberhart, D. P. Clougherty and J. M. MacLaren, *J. Mater. Res.* **8**, 438 (1993).
27. P. A. Doyle and P. S. Turner, *Acta crystallogr. A* **24**, 390 (1968).
28. F. Herman and S. Skillman, *Atomic Structure Calculations*. Prentice-Hall, Englewood Cliffs, N.J. (1963).
29. S.-H. Wei and H. Krakauer, *Phys. Rev. Lett.* **55**, 1200 (1985), and references therein.
30. A. G. Fox and C. G. Shirley, *J. Phys. F: Met. Phys.* **13**, 1581 (1983).
31. P. Georgopoulos and J. B. Cohen, *Scripta metall.* **1**, 147 (1977).
32. R. Holmestad, A. L. Weickenmeier, J. M. Zuo, J. C. H. Spence and Z. Horita, in *Proc. Electron Microscopy and Analysis Group Conf., EMAG93* (edited by A. J. Craven). Inst. Phys. Conf. Ser. No. 138, Section 3, p. 141. Institute of Physics, Bristol (1993).
33. S. A. Court, V. K. Vasudevan and H. L. Fraser, *Phil. Mag. A* **61**, 141 (1990).
34. M. J. Mehl, J. E. Osburn, D. Papaconstantopoulos, and B. Klein, *Mater. Res. Soc. Symp. Proc.* **186**, 277 (1991).
35. W. A. Shelton, D. M. Nicholson, G. M. Stocks, F. J. Pinski, D. D. Johnson, P. Sterne and W. M. Termmerman, *Mater. Res. Soc. Symp. Proc.* **186**, 113 (1991).
36. P. A. Schultz and J. W. Davenport, *Scripta metall. mater.* **27**, 629 (1992).